

Correlation of quenched structural disorder and magnetism in TiFe₂ Laves-phase thin films

J. Köble* and M. Huth

Institut für Physik, Universität Mainz, Staudinger Weg 7, D-55099 Mainz, Germany

(Received 7 May 2002; published 28 October 2002)

In recent bandstructure calculations for the *C14* Laves-phase intermetallic compound TiFe₂ two energetically nearly degenerate magnetic ground states (antiferromagnetic and ferromagnetic) were predicted. As a consequence of this near-degeneracy in the *C14* stability range of Ti_xFe_{1-x} ($x \approx 1/3$) the magnetic properties are strongly correlated with the sublattices' occupation by Ti and Fe. We analyzed the magnetic properties of a series of thin epitaxial films with varying composition in the *C14* stability range. The temperature- and field-dependent magnetic properties of these samples were determined by dc superconducting quantum interference device magnetization measurements. We found clear indications of magnetic phase separation into antiferromagnetic and ferromagnetic regions as a function of the composition. From the characteristic ordering temperatures a magnetic phase diagram for thin films in small aligning fields was established. Monte Carlo simulations based on a quenched random disorder model were performed. The resulting magnetization curves and the deduced simulated magnetic phase diagram are in good correspondence with the experimental data. We conclude that magnetic phase separation is a salient feature of Ti_xFe_{1-x} ($x \approx 1/3$). It is induced by sublattice disorder which leads to a symmetry break of the exchange field and thus favors ferromagnetic spin alignment of the unit cell.

DOI: 10.1103/PhysRevB.66.144414

PACS number(s): 75.70.Ak, 75.10.Nr, 75.50.Lk

The Laves-phase compounds exhibit a large variety of physical properties, such as heavy fermion behavior or large magnetostriction. Especially, the *LFe₂*-type Laves-phase compounds (*L* is usually a *3d* or *4f* element with a larger atomic radius than Fe) appear interesting since they may serve as prototypes for studies on the fundamental aspects of magnetic phases and their relation to structural order. These compounds exhibit a large diversity of magnetic ground states and they recently attracted interest due to newly developed methods of calculating their spin-dependent electronic band structure. As a result of such calculations, the variability of the magnetic ground states in these *LFe₂* compounds was associated with the energetic near degeneracy of different spin structures.¹⁻⁷ This may result in a strong dependence of the magnetic properties on the composition for structurally homogeneous off-stoichiometric compounds or compounds with substitution of a third kind of atoms. TiFe₂ is a prominent representative for this sensitivity to compositional variation. An accurate description of the composition-dependent magnetic properties of the complicated TiFe₂ system may yield a more general understanding of the magnetism of the *LFe₂* compounds.

For the *C14* Laves-phase TiFe₂ an energetic near-degeneracy of an antiferromagnetic (AF) and a ferromagnetic (FM) ground state was predicted by spin-resolved band structure calculations.⁴ These predictions found support by recent studies on well-prepared polycrystalline bulk samples.⁸ For these samples magnetic clustering within the *C14* phase was suggested to be responsible for the magnetic phase coexistence of antiferromagnet and ferromagnet as a function of composition about the stoichiometric point. However, iron segregation was detected for these samples which can be expected to strongly alter their magnetic properties. This is thought to be a general problem of the TiFe₂ sample preparation from the melt.⁸ Since the microscopic understanding of the antiferromagnetic/ferromagnetic coex-

istence in the TiFe₂ compound is still incomplete, an alternative approach to the TiFe₂ problem was attempted in the present work. Our analysis is based on (00*l*)-oriented TiFe₂ thin films whose preparation and structural characterization was described elsewhere.⁹ The samples' composition range is $0.24 \leq x \leq 0.42$ and the range of homogeneity (ROH) was determined to $0.28 \leq x \leq 0.39$ with no indications of Fe segregation.

The outline of this paper is as follows. Basic aspects of the TiFe₂ intermetallic compound are presented in Sec. I. The magnetic characterization, as performed by superconducting quantum interference device (SQUID) magnetometry, is described in Sec. II. The analysis of the composition-induced transition between different magnetic ground states is performed for a series of epitaxial thin films based on the magnetization data. Many issues remain unsolved within this analysis. Therefore, a microscopic model with random quenched disorder based on the 3D Ising antiferromagnet is introduced in Sec. III to gain further insight into these problems. Monte Carlo simulations were performed to establish the model's composition-dependent magnetic properties. These are compared to the experimental data. The report concludes in Sec. IV.

I. BASIC ASPECTS OF TiFe₂

The present work focuses on the Laves phase compound TiFe₂ with *C14* structure (see Fig. 1). The binary system Ti_xFe_{1-x} exhibits a relatively wide stability range for the *C14* structure between $x=0.276$ and $x=0.352$ at $T \approx 1300$ °C.¹⁰ In another work the *C14* phase was found to be stable between $x=0.285$ and $x=0.355$.¹¹ The maximum of the liquidus line occurs at the stoichiometric composition $x = \frac{1}{3}$ at $T=1427$ °C where the *C14* structure melts congruently.¹⁰ On the other hand, in a recent work the con-

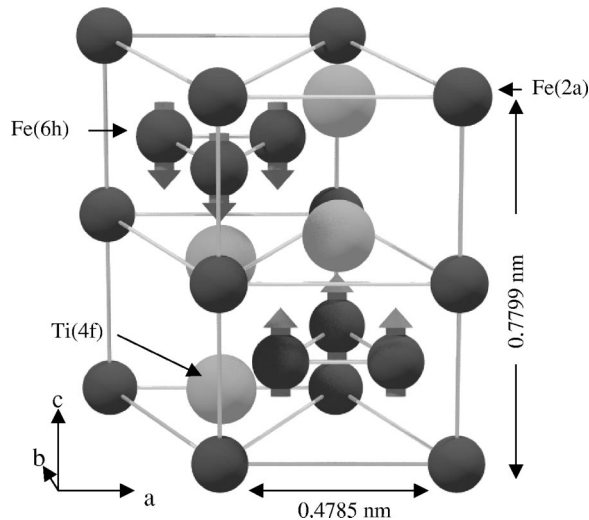


FIG. 1. Crystallographic unit cell of the hexagonal C14-Laves phase structure. The Wyckoff positions are representatively indicated by arrows. The lattice constants are $a=0.4785$ nm and $c=0.7790$ nm. The magnetic configuration of the stoichiometric compound is antiferromagnetic as indicated by the arrows on the $6h$ sites.

gruent melting point was found at $x=0.35$ and $T=1415$ °C.¹² This indicates that the range of homogeneity and the congruent melting point of the C14 structure substantially depend on the preparation method (e.g., annealing time, etc.).^{8,10–12}

The first complete description of the magnitude and the alignment of the magnetic moments on the different symmetry sites within the unit cell were given in 1992 by Brown *et al.*¹³ The configuration corresponds to an anisotropic collinear antiferromagnet as shown in Fig. 1: the magnetic moments are stabilized on the Fe($6h$) sites and are aligned parallel to the c axis in a staggered fashion; the magnetic moment amounts to $|\vec{m}_{6h}|=1.4\mu_B$ at $T=4$ K.¹³ The molecular field on the Fe($2a$) sites cancels due to site symmetry. Thus, no ordered moment on these sites is found for the stoichiometric compound. In off-stoichiometric compounds the excess atoms substitute on antisites. In this case, the symmetry is disturbed and nonzero magnetic moments are found on the Fe($2a$)- and the Fe-substituted Ti($4f$)-sites.¹⁴ The overall alignment of the moments is then ferromagnetic.

II. MAGNETIC PROPERTIES

All magnetization measurements of the samples were performed with a SHE rf-superconducting quantum interference device (rf-SQUID) magnetometer. All temperature-dependent magnetization curves presented in this section were obtained during cool down of the samples in an external magnetic field $\mu_0 H_{\text{ext}}=9$ mT from $T=285$ K to $T=5$ K. The magnetic field was applied in the film plane, i.e., perpendicular to the c axis which is the axis of easy magnetization in bulk samples.

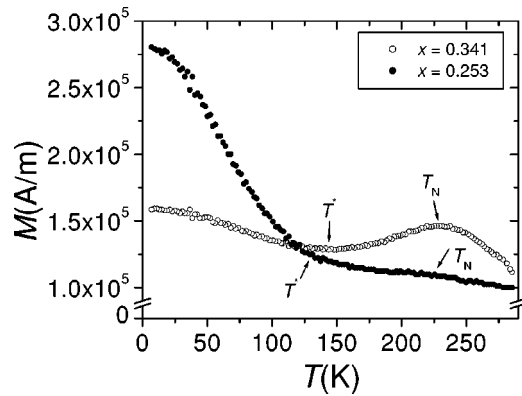


FIG. 2. Magnetization for $x=0.252$ (full circles) and $x=0.341$ (open circles). The respective ordering temperatures are marked by arrows.

A. General temperature dependence of the magnetization

We repeat that the symmetry break due to atomic substitution for off-stoichiometric compounds causes a magnetic moment to appear on the Fe($2a$) sites. The overall alignment then turns to ferromagnetic. It can be expected that off-stoichiometric compounds may also contain extended C14 regions which are ferromagnetically ordered. In Fig. 2 two typical $M(T)$ curves of a stoichiometric and an Fe-rich sample are compared. For both curves, starting from high temperatures, the magnetization increases to a local maximum which is pronounced for the stoichiometric sample and much less so for the Fe-rich sample. The temperature of this maximum is identified as the ordering temperature T_N of antiferromagnetically ordering regions in the samples. Equally pronounced for the stoichiometric sample is the subsequent drop of the magnetization to a local minimum which is due to increasing AF order in the sample. The onset of the increase of $M(T)$ at lower temperatures is measured by T^* . This increase can be related to ferromagnetically ordering regions. Consequently, the minimum between T^* and T_N is due to a superposition of a FM and AF magnetization curve and T^* is a measure for the ordering temperature of ferromagnetically correlated regions.¹⁵ For the iron-rich sample the ferromagnetlike increase is more distinct than for the stoichiometric sample. Additionally, a background magnetization persisting to the highest temperatures measured is to be noticed.

B. Influence of the sublattice order

The influence of the sublattice order on the magnetic properties is demonstrated in Fig. 3. The magnetization data of two samples with nearly the same composition but a different degree of sublattice order (induced by different deposition temperatures⁹) are compared. For the well-ordered sample, the local maximum at T_N and the increase at lower temperatures is visible, as described above. In contrast, for the less-ordered sample only FM behavior is found. This was checked for several sample pairs. The Curie temperature of the less-ordered sample is elevated as compared to the well-ordered sample. Since the sublattice order is reduced in large

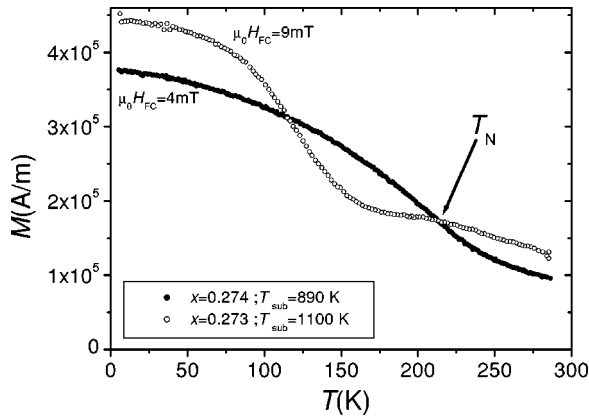


FIG. 3. Comparison of the magnetization data for films prepared at substrate temperature $T_{\text{sub}} = 890$ K with reduced sublattice order (full circles) and at the optimized temperature $T_{\text{sub}} = T_{\text{opt}} = 1100$ K with good sublattice order (open circle). The arrow indicates the position of T_N for the sample prepared at T_{opt} .

regions for samples prepared at lower temperatures, these regions are predominantly FM and the Curie temperature for these regions is increased.

C. Magnetic phase diagram

In Fig. 4 the temperature-dependent magnetization curves of all samples are shown in comparison. As is evident, the position of T^* and T_N is a function of x . For all curves, both

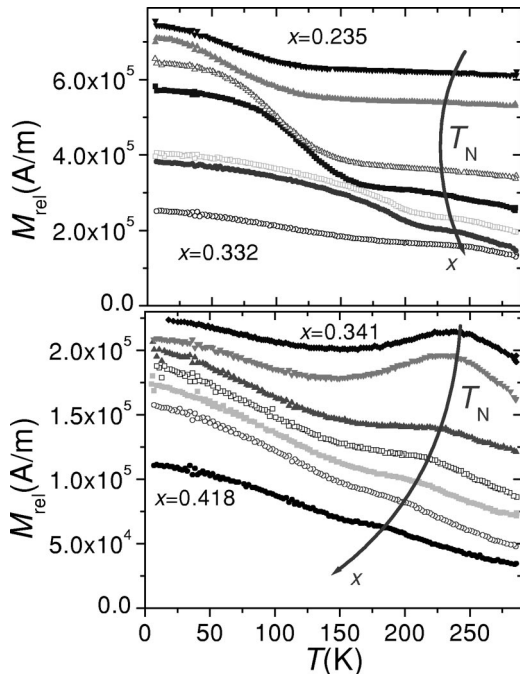


FIG. 4. Overview of the temperature-dependent magnetization curves of the epitaxial (00l)-grown sample series. The applied aligning field was $\mu_0 H_{\text{ext}} = 9$ mT. The curves are labeled with the respective Ti concentration x . The vertical curves indicate the positions of T_N . The relative magnetization values are to scale, but offsets were added to facilitate comparison. T_N for small and large x appears more distinct at appropriate scaling.

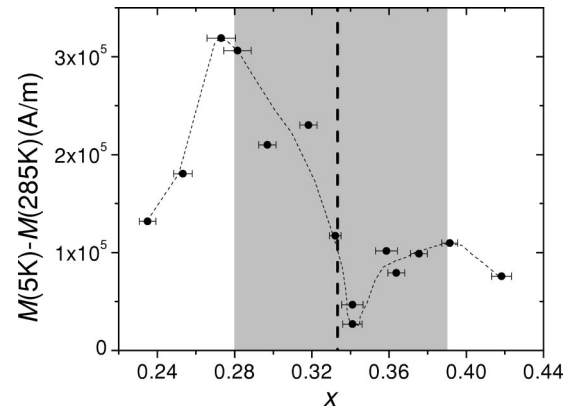


FIG. 5. $\Delta M = M(T=5 \text{ K}) - M(T=285 \text{ K})$ taken from Fig. 4. ΔM can be assumed to be proportional to the volume of ferromagnetlike regions. The shaded area represents the range of homogeneity. Dashed lines are to guide the eye.

the AF and FM contributions can be distinguished. In the range about the stoichiometric composition the maximum formed at T_N is very distinct. On decrease of x the maximum is reduced and remains only faintly visible at the iron-rich boundary of the ROH. For samples with $x > \frac{1}{3}$ the same behavior is observed, but the FM contributions appear less pronounced. In contrast to the samples at the Fe/TiFe₂ boundary, for the samples at the Ti-rich side the maximum at T_N remains clearly visible. We deduce that the ratio of the AF and FM contributions strongly depends on the composition, too.

A qualitative determination of the volume fraction of the ferromagnetlike regions in the samples was achieved by comparing the magnitude of the magnetization at lowest temperature. In the present case the excess magnetization, which is the difference between the magnetization at low temperatures and the background magnetization at high temperatures $\Delta M = M(T=5 \text{ K}) - M(T=285 \text{ K})$, is assumed to be proportional to the volume of ferromagnetlike regions. In Fig. 5 ΔM is plotted as a function of the composition. A pronounced minimum is observed at the stoichiometric point indicative of the largest contribution of AF regions. With increasing deviation from the stoichiometric composition ΔM grows, indicating an increasing volume fraction of ferromagnetlike regions. The volume increase of FM regions is strongly pronounced for the Fe-rich samples whereas it is found to be moderate for Ti-rich samples. At either boundary of the ROH a maximum of ΔM , and thus the FM volume, is found. For off-stoichiometric samples outside the ROH, ΔM decreases. This effect is pronounced for the Fe-rich samples and must be related to a structural change in the samples setting in at the ROH boundaries. For the Fe-rich boundary spontaneous segregation of Fe was found.⁹

From the data of Fig. 4 the characteristic temperatures T^* and T_N were determined. They define the phase boundaries of a magnetic phase diagram $T(x)$ which is shown in Fig. 6. In the ROH four regions can readily be identified: (1) a paramagnetic (PM) region at high temperatures, (2) an AF region, in which the ferromagnetlike contributions are paramagnetic, and (3), (4) FM*/AF and AF/FM* coexistence

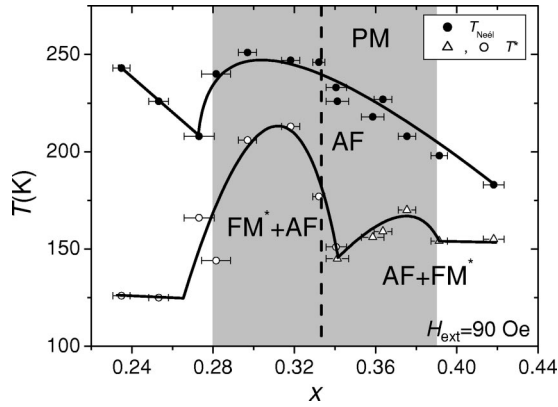


FIG. 6. Magnetic phase diagram of $\text{Ti}_x\text{Fe}_{1-x}$ (00l)-oriented epitaxial thin films in the C14 stability range. The phase boundaries were deduced from the data of Fig. 4 as indicated in Fig. 2. The shaded area represents the range of homogeneity.

regions on the Fe-rich and the Ti-rich side, respectively, in which a combined AF/FM behavior is found.

We note that the thin films' Néel temperatures are lower than $T_N^{\text{bulk}} \cong 275$ K of bulk samples.⁸ This is probably due to a finite-size induced reduction of critical temperatures. The detailed shape of the magnetic phase diagram is caused by an intricate interplay of dilution and coherence. A maximum of T_N is formed with a monotonous decrease to either side within the ROH. This decrease of T_N is caused by a dilution of the AF matrix due to Fe or Ti antisite occupation. The maximum of T_N should occur at the stoichiometric point. Nevertheless, we observed a shift to the Fe-rich region. Since T_N is also determined by the degree of crystalline coherence in the samples, the enhancement of epitaxial single crystalline growth in the iron excess region, as discussed elsewhere,⁹ competes with the reduction of T_N as a consequence of the dilution.

T^* exhibits a more complicated behavior which is dominated by clustering FM regions. Generally, in contradistinction to results obtained on bulk samples,⁸ T^* is found to be significantly lower than T_N in the whole compositional range covered by the thin film experiments. For the films this leads to the assumption that the C14 phase forms a well-stabilized antiferromagnetic matrix in which contributions of ferromagnetic C14 phase impurities with reduced T_C are embedded. These impurities are assumed to be caused by Fe or Ti atoms on antisites breaking the symmetry of the unit cell, as was found in other experiments.^{8,11,14,16}

At the stoichiometric point of the present phase diagram a local minimum of T^* is observed. This is assumed to be due to the predominant formation of the AF matrix in conjunction with small-sized FM C14 phase clusters which may form a random network. On reduction of x , not only the FM network becomes more dense but the crystalline growth is also improved. A pronounced maximum of T^* is formed at $x_{T^*_{\text{max}}} \approx 0.31$. Since the unit cell volume decreases linearly towards the Fe-rich boundary of the ROH,⁹ a segregation-free substitution process as a function of x can be assumed. The decrease of T^* for $x < 0.31$ must then be related to a reduction of the average FM C14 cluster size. Consequently,

the constant T^* in the Fe segregation region is due to a constant minimum cluster size. On the Ti-rich side, the insertion of FM impurities caused by Ti atoms on antisites is accompanied by a degrading crystalline coherence and leads to the formation of a less pronounced maximum. Again, beyond the ROH boundary T^* remains constant.

In contradistinction to the present thin film magnetic phase diagram deduced from data taken for a small aligning field of $\mu_0 H_{\text{ext}} = 9$ mT the available magnetic phase diagram for bulk samples⁸ was taken in a large magnetic aligning field of $\mu_0 H_{\text{ext}} = 1$ T. For the bulk samples different regions of FM, AF, and coexisting AF/FM order, in broad correspondence to our results, were identified. However, for the Fe-rich region a pronounced increase of T^* with decreasing x was observed. This is most likely caused by a segregation network of Fe precipitates. Such precipitates were detected by virtue of their magnetic signature at high temperatures for a set of samples analyzed by Wassermann *et al.*⁸ This network will be aligned by the large magnetic field; its coupling to the FM C14 regions may then cause a significant increase of T^* .

Moreover, for all temperatures below the PM region about the stoichiometric composition, a purely AF state exists for the bulk samples but no pure AF phase was found for the thin films. In the bulk samples Fe segregation may locally reduce the Fe concentration of the C14 phase and favor AF C14 formation, which may explain the different behavior. The structural analysis of the epitaxial thin films gives no hints for Fe precipitates in the range of homogeneity and is thus assumed to reflect the intrinsic properties of $\text{Ti}_x\text{Fe}_{1-x}$ in the C14 stability range. This is in contrast to the bulk phase diagram whose interpretation suffers from the poorly defined influence of Fe precipitates on the magnetic properties.

III. MICROSCOPIC MODEL OF MAGNETIC PHASE SEPARATION

A. Suggested model

In the previous section a composition-dependent transition from predominantly AF behavior at the stoichiometric point to AF/FM coexistence behavior for off-stoichiometric compositions was deduced for the epitaxial thin films. In the model suggested here, this transition is caused by a dilution of the antiferromagnet by an increasing number of ferromagnetically coupling impurity sites forming FM clusters. In this context, the FM coupling is induced by the substitution of Fe on Ti antisites or Ti on Fe antisites, disturbing the symmetry of the unit cell. The strong influence of this quenched disorder on the magnetic properties is thought to be a generic feature of $\text{Ti}_x\text{Fe}_{1-x}$. In the following, a Hamiltonian is suggested which considers this formation of ferromagnetically coupling impurity sites with deviations from stoichiometry.

In the suggested model a lattice site of the simulation corresponds to half the unit cell of the real crystal along the c direction which we assume to be parallel to the z axis. The coupling between these lattice sites may then be antiferromagnetic or ferromagnetic along the c axis. Thus, two different types of lattice sites are to be distinguished in the model: A sites corresponding to the AF stoichiometric composition

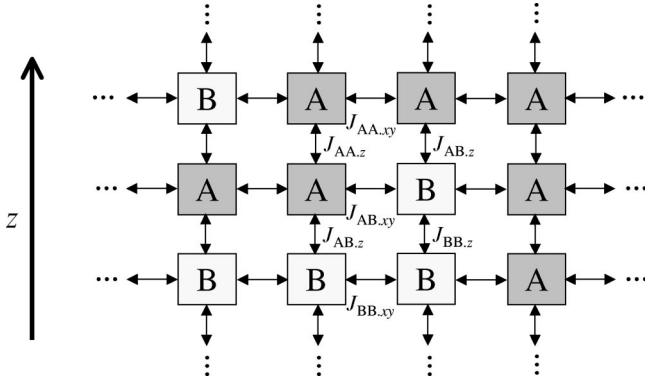


FIG. 7. Illustration of the coupling constants as introduced in the diluted antiferromagnet model. The antiferromagnetically coupling sites are denoted by A and the ferromagnetically coupling sites by B. The coupling is indicated by arrows. The figure shows a 2D cut through the 3D lattice.

and B sites for the FM off-stoichiometric composition. The A sites couple antiferromagnetically in z direction with A sites (coupling constant $J_{AA,z} < 0$) and ferromagnetically with B sites ($J_{AB,z}, J_{BA,z} > 0$). The in-plane coupling of A sites with either kind of sites is always FM ($J_{AA,xy} > 0, J_{AB,xy} > 0, J_{BA,xy} > 0$). B sites couple ferromagnetically with B sites in $x, y,$ and z directions ($J_{BB,z} > 0, J_{BB,xy} > 0$). One possible configuration is illustrated in Fig. 7. In this way, the antiferromagnetically layered structure of the Fe(6h) atom (see Fig. 1) is reproduced if the lattice consists only of A sites, as depicted at the top of Fig. 8. The off-stoichiometric compositions correspond to a partial occupation of the lattice with B sites, as illustrated at the bottom of Fig. 8.

We assume that the A and B-site occupation occurs randomly. An occupation variable c_i for each lattice site i is introduced. $c_i = 0$ if the site i is of type A and $c_i = 1$ if it is of type B. The predetermined probability distribution of the configurations $\{c_i\}$ is denoted $P\{c_i\}$. Typically, $P\{c_i\} = 1/N_{\{c_i\}}$ if $N_{\{c_i\}}$ is the number of possible configurations and

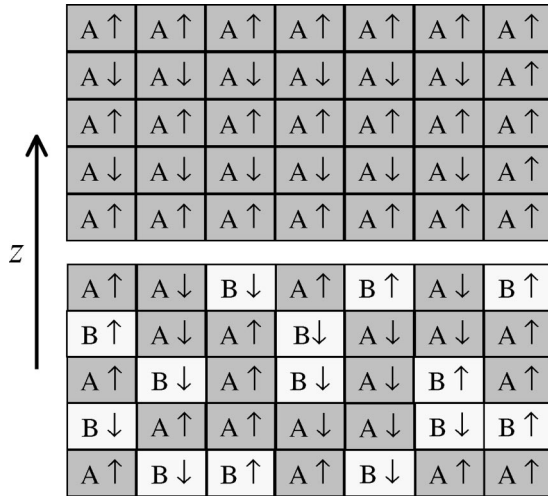


FIG. 8. Lattice configuration for the diluted antiferromagnet model. Top: Occupation probability $p = 0$ in the AF state. Bottom: $p = 0.4$ with a random orientation of the spins. See text for details. The figures show a 2D cut through the 3D lattice.

the distribution is homogeneous. The relative occupation probability p of the lattice with type B sites for a given $\{c_i\}$ is then

$$p = \frac{1}{N} \sum_i c_i. \quad (1)$$

N is the overall number of lattice sites. We assume a next-neighbor Ising-coupling of the spins $\sigma_i = \pm 1$. The general Hamiltonian for the model with spin configuration $\{\sigma_i\}$ in an external magnetic field H is then given by

$$\begin{aligned} \mathcal{H}\{\sigma_i, c_i\} = & - \sum_{\langle i,j \rangle_z} [(1-c_i)c_j J_{AB,z} + c_i(1-c_j) J_{BA,z} \\ & + c_i c_j J_{BB,z} + (1-c_i)(1-c_j) J_{AA,z}] \sigma_i \sigma_j \\ & - \sum_{\langle i,j \rangle_{xy}} [(1-c_i)c_j J_{AB,xy} + c_i(1-c_j) J_{BA,xy} \\ & + c_i c_j J_{BB,xy} + (1-c_i)(1-c_j) J_{AA,xy}] \sigma_i \sigma_j \\ & - \mu_0 \mu_B H \sum_i \sigma_i. \end{aligned} \quad (2)$$

The summation indicated by the indices $\langle i,j \rangle$ is limited to next neighbors. Via $\{c_i\}$ non-homogeneous distributions of ferromagnetically coupling sites may also be realized, e.g., clusters. From symmetry we note $J_{BA,i} = J_{AB,i}$ ($i = xy, z$).

Equation (2) is inspired by the Hamiltonian commonly used for the simulation of systems with quenched randomness, such as binary alloys prepared from the melt.¹⁷ In the present case, for the internal energy calculations the magnetic moment of a single spin was set to $|\vec{m}_\sigma| = 1 \mu_B$.

B. Simulation

The model described in the previous section was taken as a basis for classical Monte Carlo simulations employing the Metropolis algorithm¹⁸ on a 3D Ising-like lattice with dimensions $L_x \times L_y \times L_z$ ($L_x = 100, L_y = 100, L_z = 10$). Random numbers were generated by the R250/R521 generator.¹⁹ According to the definition of p [see Eq. (1)] an exact fraction $p L_x L_y L_z$ of lattice sites is occupied by ferromagnetically coupling impurity sites, representing the quenched randomness of the system. All simulations were performed in thermal equilibrium which was checked by the analysis of the autocorrelation function in long-time runs as a function of p and T . The number of subsequent Monte Carlo steps (MCS) necessary for relaxation of the spin lattice from its initial state was found to vary from 3×10^4 MCS at high temperatures to 2000 MCS at low temperatures. The mean value of the order parameter $M(T)$ at a given temperature was determined from the average of 1000 subsequent Monte Carlo steps in the relaxed state yielding a sufficiently small error. For all data points a relatively large magnetic aligning field of $\mu_0 H_{\text{ext}} = 10$ T was applied since the relaxation time significantly decreases for increasing magnetic field. However, the large aligning field was not found to significantly alter the shape of the $M(T)$ curves and the characteristic ordering temperatures since the Zeeman energy is still small as com-

TABLE I. Standard coupling constants determined from heuristic principles (see text for details).

	xy	z
AA	11.9 meV	-2.0 meV
AB	5.0 meV	2.0 meV
BB	5.0 meV	2.0 meV

pared to the chosen coupling constants. All simulations were performed using periodic boundary conditions.

First, the large number of parameters must be reduced to an appropriate subset of physically relevant parameters. The magnitude of the coupling energies can be expected to be in the range known for simple magnetic materials. The relevant parameter space was systematically screened for agreement of the resulting magnetization curves with the experimental data (see Sec. II). In order to obtain $T^* < T_N$, as observed experimentally, the in-plane coupling constants $J_{AB,xy}$ and $J_{BB,xy}$ have to be reduced with respect to $J_{AA,xy}$. AF/FM coexistence behavior was only found for weak coupling along the anisotropy axis (see Table I).

Due to the quenched randomness introduced by the additional random variable $\{c_i\}$, which is kept fixed during the simulation, an additional averaging has to be carried out over the distribution $P\{c_i\}$ of $\{c_i\}$ (Ref. 17)

$$[\langle M\{\sigma_i, c_i\} \rangle_T]_{av} = \int d\{c_i\} P\{c_i\} \frac{1}{Z\{c_i\}} \text{Tr}_{\sigma_i} (M\{\sigma_i, c_i\} \times \exp[-\mathcal{H}\{\sigma_i, c_i\}/k_B T]) \quad (3)$$

with the partition function $Z\{c_i\}$ of the configurations $\{c_i\}$ and the spin configurations $\{\sigma_i\}$. The squared brackets on the left indicate this additional average over the $\{c_i\}$, whereas the thermal average is indicated by the subscript T . Consequently, several magnetization curves with constant p but random $\{c_i\}$ were simulated, i.e., Metropolis importance sampling was performed for the thermal average $\langle \dots \rangle_T$ and simple sampling for the configuration average $[\dots]_{av}$. Another problem is generated by multiple near-degenerate minima of the free energy as is also found for spin glasses.¹⁷ The relaxation to the absolute minimum is very slow at low temperatures and the necessary computation time thus becomes very large. However, the double averaging described above and performed by averaging over multiple magnetization curves may also help to find the absolute minimum. In the present simulations an average over ten simulated magnetization curves with different random $\{c_i\}$ at constant p was found to sufficiently reduce the standard error of the arithmetic mean value which represents the absolute minimum of the free energy. Finite size effects were analyzed briefly by examining the behavior of larger lattices up to $200 \times 200 \times 20$ lattice sites. Within the limits of the given temperature resolution no deviations of the general shape of the curves were observed. For the classical Ising system it is known that for the examined lattice sizes finite size effects alter the shape of the magnetization curves only marginally with respect to the analytical solution. Furthermore, an in-

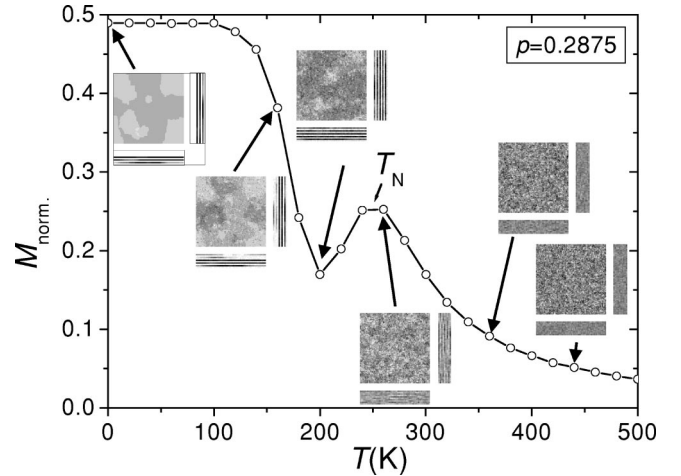


FIG. 9. $M(T)$ and spin structure for $p=0.2875$. The 3D images show a combined view of the spin configuration from top, front and side with averaging about the viewers direction, which is mapped to a gray scale. The z axis has been rescaled. As can be seen, FM domains are formed at the onset of ferromagnetism and maintained to low temperatures. The shape of the $M(T)$ curves strongly varies for different simulations with identical configurations $\{c_i\}$.

crease of the lattice size was found to not significantly help reducing the necessary multiple curve averaging by self-averaging. As is known from the analysis of the order parameter about T_C for systems with quenched randomness^{17,20} a lack of self-averaging occurs. This was also found for the present model.

C. Comparison of simulation and experiment

In Fig. 9 a representative $M(T)$ curve of a sample simulation for $p=0.2875$ and random $\{c_i\}$ is shown, in conjunction with the corresponding spin structure at various temperatures. Starting at high temperature a paramagnetic region with completely disordered spin structure is found. Despite an increase of the induced magnetization, no significant order is seen in the top view on approaching $T_N \approx 257$ K. Nevertheless, the side views already reveal the onset of a lateral spin order with alternating planes. At the local minimum (T^*) the AF structure appears very distinct in the side views. In the top-view large regions with increased brightness indicate large net magnetizations due to FM clusters. Further decrease of the temperature causes these regions to stabilize. The easy alignment of the ferromagnetically ordering regions by the magnetic field results in a further increase of the brightness. From the side views it can be seen that these domains are virtually two dimensional. At the lowest temperature $T=0.1$ K the whole lattice is separated into FM and AF domains. It is noteworthy that the FM domains stay fixed at the position where they were initially formed. Finally, the domain structure for a given configuration $\{c_i\}$ and thus the low temperature magnetization varies from simulation to simulation, caused by the multiple minima energy landscape.

The simulation data for various p values are shown in Fig. 10. For $0 \leq p \leq 0.26$ antiferromagnetic ordering was observed exclusively (only $p=0.26$ shown). The transition from predominantly AF to FM behavior sets in at $p > 0.28$, indicated

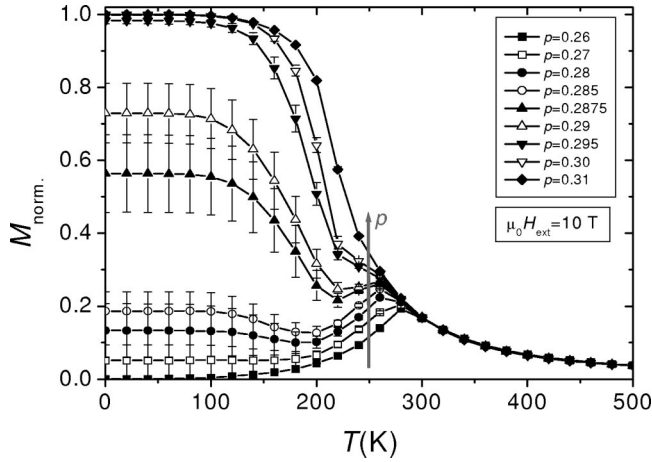


FIG. 10. Arithmetically averaged $\bar{M}(T)$ of ten simulations with different $\{c_i\}$ but constant p . The error bars are the standard error of the mean value.

by a pronounced increase of $M(T)$ at lower temperatures. At $p=0.31$ the magnetization data exhibits an almost FM shape and is completely saturated below $T=100$ K. The width of the transition is $\Delta p=0.03$.

As can be seen in Fig. 11 the shape of the experimental $M(T)$ curves with the local maximum at T_N and the local minimum at T^* is reproduced for the nearly stoichiometric composition at $x=0.34$ and the iron-rich composition at $x=0.32$. The ratio of T_N and T^* is equal to the corresponding

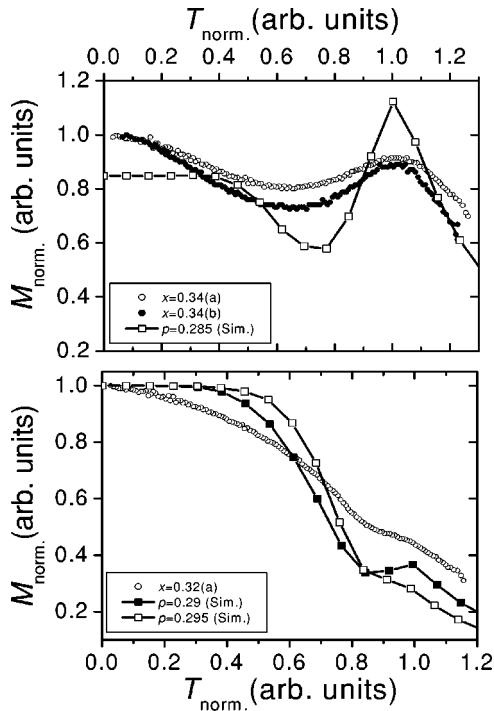


FIG. 11. Comparison of simulated and experimental magnetization data. Top: $M(T)$ taken from two different samples with $x=0.34$ compared against the $p=0.285$ curve of Fig. 10. Bottom: $M(T)$ taken from a sample with $x=0.32$ compared against $p=0.29$ and $p=0.295$. The curves were rescaled to facilitate comparison.

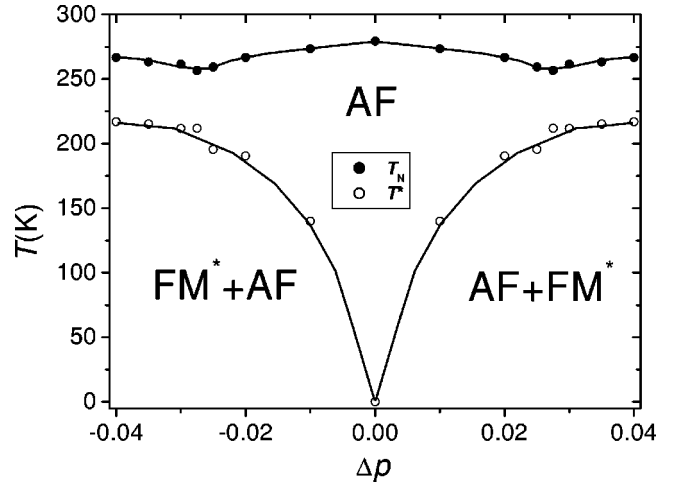


FIG. 12. Simulated phase diagram with the characteristic temperatures determined from the data of Fig. 10. To facilitate a comparison with the experimental data (see Fig. 6) the characteristic temperatures were drawn symmetrically to either side of the diagram for the simulation data. The phase identities for the simulation data were chosen in correspondence to the naming chosen in the analysis of the experimental data.

value of the experimental data for $x=0.32$ whereas T^* of the simulation seems to be slightly larger for $x=0.34$. It has to be noticed that the slope at the onset of ferromagnetism is larger in the simulations which is due to the simplifying assumptions of the Ising model.

D. Comparison of the phase diagrams

As detailed in Sec. II C, a magnetic phase diagram was determined from the characteristic temperatures observed in the $M(T)$ data of the epitaxial samples. We now compare this experimental phase diagram to the simulation results. From the simulation data of Fig. 10 the critical temperatures T_N and T^* were determined in accordance with the procedure used for the experimental data. The resulting phase diagram is depicted in Fig. 12. Δp denotes the deviation from $p=0.26$ which corresponds to the largest p -value generating a purely AF curve. $\Delta p=0$ is identified with a stoichiometric TiFe_2 sample exhibiting a minimum amount of disorder. According to the symmetry properties of the present model and to facilitate a comparison with the experimental data of Fig. 6 the determined critical temperatures are drawn symmetrically to either side of the diagram. The corresponding phase names, as identified for the experimental data, were added to the diagram.

If it is assumed that the variable $(x - \frac{1}{3})$ of the experimental data corresponds to Δp of the simulations we are able to compare both phase diagrams. The overall behavior of T^* and T_N is reproduced well by the simulations for $0.30 < x < 0.38$. An absolute maximum of T_N is observed in this range. The absolute minimum of T^* is found consistently at $(x = \frac{1}{3})$ corresponding to $\Delta p=0$. The decrease of T_N and the increase of T^* with increasing impurity concentration is also reproduced by the simulations.

Nevertheless, the simulated phase diagram also shows significant deviations from the experimental. Considering the

limitations of the underlying model these deviations can be explained by the complex growth-related effects. For the Ti-rich region (corresponding to positive Δp in Fig. 12) the experimental temperatures T^* and T_N are significantly lower due to the reduced crystalline coherence of the samples. The shift of the maximum of T_N with respect to the stoichiometric point of the experimental phase diagram is growth-induced as well. Outside the range $0.30 < x < 0.38$ the properties of the film growth influence the critical temperatures of the thin film phase diagram in a very complex manner. The observed increase of T_N in the simulations for large Δp is most probably an artifact of our method to determine T_N which shifts the nominal T_N to larger values for large Δp .

Finally, $T^* > 0$ K for $x \approx \frac{1}{3}$ indicates that a minimum number of FM clusters is always present in the epitaxial samples, either induced by growth defects or by unavoidable small fluctuations of the deposition rate. Significant FM contributions in the simulation data are only seen above $p \approx 0.285$.

IV. CONCLUSION

The present work has shown that it is indeed possible to overcome the preparational difficulties of TiFe_2 bulk samples by the alternative approach of epitaxial thin film preparation. This approach enhances the range of homogeneity of the C14 phase.⁹ In view of the magnetic phase diagram derived here for phase-pure C14 samples, the magnetic phase diagram for bulk samples, as suggested by Wassermann *et al.*,⁸ may be significantly influenced by impurity phase segregation. The thin film phase diagram established in the present work, corrected for thin-film specific signatures, can be assumed to be applicable to phase-pure C14 bulk samples as well. Nevertheless, it might be impossible to prepare such bulk samples at all due to the complicated metallurgy.

Based on the magnetic properties of the thin films and the results of the Monte Carlo simulations we conclude that the magnetism of the TiFe_2 system is mainly driven by magnetic phase separation which is induced by inhomogeneities in structure and/or composition. The energetically near-degenerate AF and FM ground states of TiFe_2 render this system highly susceptible to such a phase separation scenario. Even if it is possible to prepare structurally phase-pure samples, as shown for the epitaxial thin films, it remains questionable whether magnetically phase-pure material can be obtained. Naturally, these conclusions may be valid not only for TiFe_2 but also for other magnetic compounds exhibiting a magnetic instability due to a near degeneracy of magnetic states.

The presented simulation results propose a static magnetic phase separation driven by magnetic impurities of a predetermined concentration fixed to the lattice. However, these results do not rule out that the magnetic “granularity” of $\text{Ti}_x\text{Fe}_{1-x}$ may have aspects of a dynamic phenomenon,^{21–25} as was predicted for diluted ferromagnets in the context of a Griffith phase.²¹ If this were the case, the magnetic phase separation would be generated by fluctuating AF/FM spin clusters. Spin-polarized STM measurements could then be employed to determine the degree of (quasi)static magnetic phase separation in TiFe_2 . Alternatively, fast probes, such as spin-polarized magnetic neutron scattering, could give insight into the degree of dynamic phase separation. This has to remain for future resolution.

ACKNOWLEDGMENTS

The authors wish to thank the MWFZ Mainz for financial support and Dr. W. Paul (Mainz) for advice with the Monte Carlo simulations.

*Electronic address: j.koebler@omicon.de

¹S. Asano and S. Ishida, *J. Magn. Magn. Mater.* **70**, 39 (1987).

²S. Asano and S. Ishida, *J. Phys. F: Met. Phys.* **18**, 501 (1988).

³S. Asano and S. Ishida, *J. Phys.: Condens. Matter* **1**, 8501 (1989).

⁴E. Hoffmann, P. Entel, E. Wassermann, K. Schwarz, and P. Mohn, *J. Phys. IV*, C2-117 (1995).

⁵S. Ishida, S. Asano, and J. Ishida, *J. Phys. Soc. Jpn.* **54**, 4695 (1985).

⁶S. Ishida and S. Asano, *J. Phys. Soc. Jpn.* **54**, 4688 (1985).

⁷S. Ishida, S. Asano, and J. Ishida, *J. Phys. Soc. Jpn.* **54**, 3925 (1985).

⁸E.F. Wassermann, B. Rellinghaus, T. Roessel, and W. Pepperhoff, *J. Magn. Magn. Mater.* **190**, 289 (1998).

⁹J. Köble and M. Huth, *J. Cryst. Growth* **234**, 666 (2002).

¹⁰*Binary Alloys Phase Diagrams*, edited by T.B. Massalski (ASM International, Materials Park, OH, 1996).

¹¹W. Brückner, K. Kleinstück, and G.E.R. Schulze, *Phys. Solid State* **23**, 475 (1967).

¹²P. Stauche, S. Erdt-Böhm, M. Brinkmann, and H. Bach, *J. Cryst. Growth* **166**, 390 (1996).

¹³P.J. Brown, J. Deportes, and B. Ouladiaz, *J. Phys.: Condens. Matter* **4**, 10 015 (1992).

¹⁴G.K. Wertheim, J.H. Wernick, and R.C. Sherwood, *Solid State Commun.* **7**, 1399 (1969).

¹⁵An exact determination of the ordering temperature T_C from the magnetization data would only be possible by exactly modeling the complete curves.

¹⁶J. Pelloth, R.A. Brand, and W. Keune, *J. Magn. Magn. Mater.* **140-144**, 59 (1995).

¹⁷D.P. Landau and K. Binder, *A Guide to Monte Carlo Simulations in Statistical Physics* (Cambridge University Press, Cambridge, UK, 2000).

¹⁸N. Metropolis, A.W. Rosenbluth, M.N. Rosenbluth, A.M. Teller, and E. Teller, *J. Chem. Phys.* **21**, 1087 (1953).

¹⁹A. Heuer, B. Duenweg, and A.M. Ferrenberg, *Comput. Phys. Commun.* **103**, 1 (1997).

²⁰S. Wiseman and E. Domany, *Phys. Rev. E* **52**, 3469 (1995).

²¹R.B. Griffiths, *Phys. Rev. Lett.* **23**, 17 (1969).

²²B.M. McCoy, *Phys. Rev. Lett.* **23**, 383 (1969).

²³J.F. Dillon, Jr., E.Y. Chen, and H.J. Guggenheim, *Solid State Commun.* **16**, 371 (1975).

²⁴C. Binek and W. Kleemann, *Phys. Rev. Lett.* **72**, 1287 (1994).

²⁵C. Binek, M.M.P. de Azevedo, W. Kleemann, and D. Bertrand, *J. Magn. Magn. Mater.* **140-144**, 1555 (1995).